Spatial Channel Degrees of Freedom for Optimum Antenna Arrays

Yingke Huang, Petros Karadimas, and Abed Pour Sohrab

***Abstract*—One of the ultimate goals of future wireless networks is to maximize data rates to accommodate bandwidth-hungry services and applications. Thus, extracting the maximum amount of information bits for given spatial constraints when designing wireless systems will be of great importance. In this paper, we present antenna array topologies that maximize the communication channel capacity for given number of array elements while occupying minimum space. Capacity is maximized via the development of an advanced particle swarm optimization (PSO) algorithm devising optimum standardized and arbitrarily-shaped antenna array topologies. Number of array elements and occupied space are informed by novel heuristic spatial degrees of freedom (SDoF) formulations which rigorously generalize existing SDoF formulas. Our generalized SDoF formulations rely on the differential entropy of three-dimensional (3D) angle of arrival (AOA) distributions and can associate the number of array elements and occupied space for any AOA distribution. The proposed analysis departs from novel closed-form spatial correlation functions (SCFs) of arbitrarily-positioned array elements for all classes of 3D multipath propagation channels, namely, isotropic, omnidirectional, and directional. Extensive simulation runs and comparisons with existing trivial solutions verify correctness of our SDoF formulations resulting in optimum antenna array topologies with maximum capacity performance and minimum space occupancy.**

***Index Terms*—Antenna arrays, channel capacity, spatial correlation function, spatial degrees of freedom.**

I. Introduction

ANTENNA arrays play a dominant role on the enhancement of achievable data rates and received signal quality in 5G and beyond 5G (B5G) wireless communication networks [1]. In multi-input, multi-output (MIMO) wireless systems, spatially separated antennas are employed at both the transmitter (Tx) and/or receiver (Rx) exploiting spatial diversity, thus improving channel capacity and ensuring data reliability [2]. Therefore, exploiting the spatial characteristics of wireless propagation channels is of paramount importance for future MIMO system designs. Deriving spatial correlation enables accurate performance analysis of MIMO wireless systems [3]. In particular, spatial correlation has significant impacts on MIMO channel capacity performance [4]. In this paper, we realize optimum antenna array topologies by maximizing the ergodic MIMO channel capacity. With the aid of analytical spatial degrees of freedom (SDoF) formulations, such antenna arrays occupy minimum space. The SDoF indicates the number of independent spatial transmission modes incurred by the wireless propagation environment according to [5]. The signal-to-noise ratio (SNR) has to be sufficiently high in order the MIMO system and accordingly the ergodic MIMO channel capacity to be degrees of freedom (DoF) limited rather than power limited [6]. The presented findings can constitute a roadmap for future antenna array designs towards implementing 6G wireless systems with volumetric spectral efficiency [7] and adopting 3D antenna arrays in 3GPP standardization efforts [8]. In following sub-sections, we review the literature on the major technical challenges of the presented work, namely, closed-form spatial correlation functions (SCFs), antenna array optimization, and SDoF formulations.

Manuscript received Jan 22, 2022. This work was partially supported by the Engineering and Physical Sciences Research Council (EPSRC) under Grant EP/R041660/1: Bandwidth and Energy Efficient Compact Multi-Antenna Systems for Connected Autonomous Vehicles.

Yingke Huang and Abed Pour Sohrab were with the James Watt School of Engineering, Unviversity of Glasgow, Glasgow G12 8QQ, Scotland, U.K. (Email: yingke.huang123@gmail.com; poursohrab@gmail.com).

Petros Karadimas is with the School of Computing, Engineering and the Built Environment, Edinburgh Napier University, Edinburgh EH10 5DT, Scotland, U.K. (Email: p.karadimas@napier.ac.uk).

A. Spatial Correlation and Antenna Arrays

The SCF depends on the antenna array geometry, antenna element spacing, and wireless propagation AOA characteristics [9]. To avoid complicated numerical integrations, deriving closed-form SCFs has attracted great interests for years [3], [9]–[14]. Uniform [9]–[12] and Gaussian [13], [14] have been among the most widely adopted AOA distributions to account for wireless propagation and scattering. In uniform distributions, closed-form SCFs were determined for uniform linear array (ULA), uniform circular array (UCA), and uniform rectangular array (URA) based on the Jacobi-Anger expansion (JAE) approximation [9]. Using the same approach, closed-form SCFs were derived in [10] applicable to arbitrarily-positioned antenna array elements, however, the results were actually demonstrated for circular arrays. As presented in [9], [10], the JAE provides a straightforward implementation in evaluating the SCF. By using an alternative approach based on the spherical harmonic expansion of plane-waves, closed-form SCFs were obtained in [11] being adaptable to standardized three-dimensional (3D) arrays, and in [12] being independent of array geometries. In Gaussian distributions, various approximation methodologies were also developed for closed-form SCF solutions [13], [14]. The JAE-based method was adopted in [13] for two-dimensional (2D) arrays, while a Gaussian closed-form (GC) approximation was considered in [14] being valid for small AOA ranges. Moreover, [14] proposed a Gauss-Hermite quadrature (GHQ)-based method approximating the SCF under 2D propagation scenarios. It was concluded in [14] that the GHQ-based approximation outperforms the JAE-based and GC approaches with lower computation and higher accuracy.

Inherently, 3D arrays are more condensed compared with linear and circular ones to achieve similar performance [15]. Compared with customized 3D array topologies such as cylindrical [3], polyhedral [11], and spherical [16], an arbitrary 3D array could potentially occupy less space by letting the elements be located randomly and not just on the surface. It is an objective of this work to investigate such potential. Arbitrary array positioning constitutes a very challenging problem, e.g., see [17] for arbitrary ULA positioning via mechanical rotation or electronic selection and [18] for arbitrary element positioning in rectangular arrays. Accordingly, we derive generalized closed-form SCFs suitable for any class of 3D arrays including customized and arbitrarily-shaped. We consider 3D spherical array topologies and devise arbitrarily-shaped 3D arrays by releasing the limitation of letting the elements be located on the spherical surface. However, simulation results demonstrate that the elements of optimized arbitrarily-shaped 3D arrays tend to be located on the spherical surface. Adapting the generalized SCFs into 2D array topologies, we find that ULAs and UCAs have almost identical performance with their optimized counterparts. Such findings can be very important to guide future research towards designing uniform/symmetrized 3D arrays with identical performance with respect to their optimized arbitrarily-shaped counterparts.

In this paper, 3D directional, 3D isotropic, and 3D omnidirectional propagation scenarios [19]–[22] are considered for holistically analyzing both standardized and arbitrarily-shaped antenna array topologies. The directional scenarios are modeled via 3D restricted uniform and 3D Gaussian AOA distributions. A 3D restricted uniform AOA has unlimited flexibility to theoretically model any propagation scenario, as arbitrary scattering can be modeled by the summation of weighted uniformly distributed elementary solid-angle contributions [12], [19], whereas a 3D Gaussian AOA is a very classical model for directional propagation [21]. 3D omnidirectional scenarios, accounting for propagation in urban environments, include the pairs uniform-restricted uniform [19] and uniform-Gaussian [20], [22] AOA distributions on azimuth-elevation planes, respectively. By leveraging the JAE-based approach, we derive a closed-form SCF for 3D restricted uniform scenarios similar to the one in [10] employing the 3D AOA model of [19]. Extending the GHQ-based method presented in [14], which applies in 2D scenarios, we derive a novel closed-form SCF for 3D directional Gaussian scenarios. A novel closed-form SCF for the 3D omnidirectional scenario with Gaussian in elevation and uniform in azimuth AOA is also derived by combining the JAE- and GHQ-based techniques.

B. Antenna Array Optimization Techniques

Given space limitations, finding the optimum topologies to minimize spatial correlation and maximize channel capacity constitutes a major challenge in antenna array designs. Intelligent methodologies, such as applying evolutionary metaheuristic optimization algorithms, have been validated and resulted in antenna arrays that considerably outperform conventional ones with half a wavelength spacing [23]. Previous works [10], [24]–[26] have demonstrated the effectiveness of employing optimization algorithms to realize antenna arrays with maximum channel capacity. The particle swarm optimization (PSO) [10], [25] and genetic algorithm (GA) [24] were employed producing optimized 2D arrays such as linear and circular ones. The differential evolution (DE) algorithm was adopted in [26] to optimize cubical arrays but without maximizing channel capacity. In [16], optimum design of spherical, cubical, and half-elliptic arrays was demonstrated by using GA. The design of optimum spherical and arbitrarily-shaped 3D arrays with maximum capacity has been insufficiently addressed in these works. None of the above-mentioned works have considered the required space occupancy of antenna arrays with given numbers of elements and in any class of propagation scenario.

In this paper, we adopt the PSO algorithm to solve the previously described capacity maximization problem for the following reasons. The design of optimum antenna arrays is well known to be a highly nonlinear and nonconvex programming problem [27]. PSO can solve complex and multidimensional problems without restricting the solution domain and does not need to consider convexity. Such features make PSO a perfect candidate for nonconvex problems [28]. Besides that, compared with other evolutional optimization algorithms, PSO has fewer operators to deal with, leading to computational cost reduction and simpler implementation [29]. The work in [30] verified that within the same computation time, PSO outperforms the DE, invasive weed optimization and GA with respect to the achieved fitness. Also in [25], the PSO outperformed the GA with respect to convergence speed and accuracy. Moreover, PSO shows flexibility in controlling the balance between local and global explorations [28] and can easily obtain a rapid convergence speed by applying a time varying inertia weight [29]. An advanced PSO algorithm namely PSO with velocity mutation (PSOvm) was introduced in [30]. The PSOvm induces the mutation on the particle's velocity to improve the particle's position at the first few iterations and thus further boosts the overall algorithm performance compared with the conventional PSO [30]. Therefore, the PSOvm is selected as the state-of-art PSO technique to realize antenna array topologies with maximum capacity.

C. Spatial Degrees of Freedom

The minimum required space to achieve maximum capacity will be informed by the SDoF determined in all 3D propagation scenarios. Analytically derived SDoF formulations and minimum occupied space will be rigorously associated. The work in [31] associated SDoF to MIMO antennas where the channel capacity was limited by SDoF. A sufficiently high SNR is required in order the channel capacity to be DoF limited rather than power limited [6]. The works in [32], [33] estimated the DoF via the rank of the channel correlation matrix but without relating it to actual AOA distributions. A more accurate DoF estimation can be determined by evaluating the eigenvalues of spatial correlation matrices as in [34], [35], showing reduction of significant eigenvalues after a certain bound dictated by the DoF. The DoF formulations derived in [15] as the product of the AOA solid angle range, i.e., the SDoF, and array aperture size, rigorously determined the

maximum number of antenna elements leading to optimum capacity. Inversely, the minimum occupied space can be determined by the SDoF with given the number of antenna elements. An emerging question, not addressed in [15], is how we can locate the elements in space for achieving maximum ergodic MIMO channel capacity. The PSOvm technique, as was previously justified, addresses this issue. The AOA solid angle range considered in [15] cannot incorporate the intrinsic AOA characteristics of propagation environments. Such consideration is just valid for 3D uniform AOA scenarios as will be demonstrated and verified in Sections IV and VI.

In this paper, we heuristically derive the SDoF by adapting the information theory metric of differential entropy [36] into 3D AOA distributions. We show that the SDoF outcome in [15], i.e., the AOA solid angle range, is equivalent to our SDoF formulations for 3D uniform AOA distributions. In other words, assigning a uniform distribution in the designated 3D AOA range results in equal SDoF as the ones in [15]. We leverage such finding by extending it to any other AOA distribution and we confirm correctness by demonstrating ergodic MIMO channel capacity performance compliance when the DoF in different AOA scenarios are equal. 3D Gaussian AOA distributions are selected as case studies to demonstrate performance compliance with the 3D uniform ones. However, our SDoF formulations are generic that can be readily extended to more complex wireless propagation scenarios, such as multi-clustered ones [19] modeled via multi-modal restricted uniform or Gaussian distributions. Exploiting the SDoF formulation methodology described previously is sufficient to determine the minimum occupied space with given numbers of array elements. By running the optimization algorithm, this work results in optimum antenna array topologies with maximum capacity and minimum occupied space.

D. Contributions

Building on our very primitive simulation results published in a conference paper [37], the main contributions of this work are summarized as follows. 1) To mitigate numerical integration complexities, novel closed-form SCFs are derived based on a generic system modeling for arbitrary positioning of antenna array elements [10], [19]. Note that SCFs are necessary for MIMO channel capacity calculations. Thus, closed-form SCFs can also mitigate the complexity of ergodic MIMO channel capacity calculations ending up with simpler, but still correct, PSOvm implementations, as long as the closed-form SCFs comply with the accurate numerically-determined integration solutions. The JAE-based approach is leveraged to derive a closed-form SCF in 3D restricted uniform scenarios. We derive a novel closed-form SCF in 3D Gaussian scenarios extending the GHQ-based approach presented in [14]. Combining the GHQ- and JAE-based approaches, we further derive a novel closed-form SCF in 3D omnidirectional scenarios with uniform in azimuth and Gaussian in elevation AOA. All closed-form SCFs show outstanding agreement with their respective numerically determined SCFs. 2) The SDoF subtended by the wireless propagation scenario, through its AOA characteristics, are heuristically and generically derived for any such scenario, i.e., isotropic, directional, omnidirectional. Such SDoF formulations, relying on the differential entropy of 3D AOA distributions, are validated through performance analyses of antenna array topologies with known SDoF outcomes, i.e., linear, circular, and spherical [15]. Our SDoF formulations can be applicable to any 3D AOA distribution and not just uniform ones as in [15]. 3) Optimized antenna array topologies informed by the information theory concepts of AOA differential entropy and SDoF are presented. The SDoF metric is explicitly associated to the minimum space occupied by the antenna array for achieving maximum ergodic MIMO channel capacity. The optimized linear and circular topologies show almost identical performance with the standardized uniform topologies in all 3D propagation scenarios. Thus, knowledge of SDoF is sufficient to realize customized uniform linear and circular arrays without running time and resource consuming optimizations. The optimization outcomes also demonstrate that arbitrarily-shaped 3D arrays occupy the same space as spherical ones achieving maximum ergodic MIMO channel capacity. Employing the SDoF formulations informs the realization of such 3D arrays occupying minimum space.

E. Paper Outline and Notations

The rest of the paper is organized as follows. Section II presents the MIMO channel model and its ergodic channel capacity evaluation (II.A), followed by the antenna array model that can accommodate arbitrarily-positioned elements (II.B). Then, different wireless propagation AOA scenarios including 3D isotropic, 3D directional, and 3D omnidirectional ones are presented (II.C). In Section III, we derive closed-form SCFs for each scenario as classified in Section II.C. The SDoF formulas in [15] for linear, circular, and spherical arrays are reviewed in Section IV, followed by the derivations of generalized heuristic SDoF formulations applicable in any propagation scenario. Section V introduces the adopted PSOvm algorithm. In Section VI, we demonstrate the feasibility and correctness of the presented analysis and methodology, i.e., closed-form SCFs and SDoF formulations, towards devising optimum antenna array topologies via extensive simulation runs and comparisons. Finally, the paper is concluded in Section VII.

Main notations used in the paper are summarized in the following. We assume a MIMO wireless channel with a transmit antenna array of N_t elements and a receive array of N_r elements. $\mathbf{H}$ and $\mathbf{H}_\omega$ denote the $N_r \times N_t$ MIMO channel matrix of a Rayleigh fading channel and the $N_r \times N_t$ stochastic matrix comprised of independent identically distributed (i.i.d.) complex Gaussian entries with zero mean and unit variance, respectively. $\mathbf{R}_{rx}$ and $\mathbf{R}_{tx}$ are the $N_r \times N_r$ and $N_t \times N_t$ spatial correlation matrices of antenna arrays at the Rx and Tx, respectively, while $R_s(m,n)$ denotes the (m,n) entry of $\mathbf{R}_{rx}$/$\mathbf{R}_{tx}$, i.e., the spatial correlation between the m-th and n-th array elements. $\mathbf{I}_a$ denotes an $a \times a$ identity matrix. P/σ_n^2 is the SNR, with P the total transmitted power and σ_n^2 the noise variance. We denote $\theta \in [-\pi/2, \pi/2]$, $\phi \in [-\pi, \pi]$ as

the elevation and azimuth AOA, respectively. λ is the carrier wavelength. We denote Ω as the solid angle, $|\Omega|$ the SDoF, i.e., a metric characterizing the spatial diversity of the wireless propagation channel, and X the DoF arisen by the SDoF multiplied by the antenna aperture size [15].

II. System Model

A. MIMO Channel Model and Ergodic Capacity

The complex signal vector received at the Rx side is given by [38]

$$\mathbf{y} = \mathbf{H}\mathbf{s} + \mathbf{n} \tag{1}$$

where $\mathbf{s}$ denotes the transmitted signal vector, and $\mathbf{n}$ is the received additive white Gaussian noise vector consisting of i.i.d. entries with zero mean and unit variance. We adopt the Kronecker model to evaluate the MIMO channel matrix incurring independent correlation analyses at the Tx and Rx antennas [39]. $\mathbf{H}$ can thus be written as [39]

$$\mathbf{H} = (\mathbf{R}_{rx})^{1/2}\mathbf{H}_{\omega}(\mathbf{R}_{tx})^{1/2}. \tag{2}$$

Using the Kronecker model, we focus on the spatial correlation and array design at one side, i.e., the Rx side, by assuming the array elements at the Tx side to be uncorrelated, i.e., $\mathbf{R}_{tx} = \mathbf{I}_{N_t}$ in (2). Such assumption enables the DoF behavior to incorporate the wireless propagation environment (through its AOA characteristics) and antenna array space in accordance with [15].

Assuming that the channel state information (CSI) is unknown to the transmitter while being fully known to the receiver, the ergodic MIMO channel capacity in bits/s/Hz is given by [40]

$$C = E\left\{\log_2\left[\det\left(\mathbf{I}_{N_r} + \frac{P}{\sigma_n^2 N_t}\mathbf{H}\mathbf{H}^H\right)\right]\right\} \tag{3}$$

where the superscript "H" denotes the complex conjugate transpose, and "det" denotes the determinant operation. We define $\mathbb{H}$ as the set of channel realizations $\mathbf{H}$, thus, the expectation in (3) operates on the instantaneous capacities evaluated in each channel realization $\mathbf{H} \in \mathbb{H}$. Note that, we compute the ergodic MIMO channel capacity using (3) with the aid of (2), instead of considering full CSI at the transmitter and receiver as in [15]. This is because full CSI informing power allocation for each sub-channel is more complex and hardly feasible. However, the DoF outcome of [15] can be readily characterized by adopting (3) with performance behavior indicated by 3D uniform AOA distributions as will be demonstrated in Section VI. The presented analysis can consider other MIMO channel models including the one in [41] formed by the single side (Tx and Rx) spatial correlation matrices.

B. Antenna Array Element Positioning

The spatial correlation is characterized by the array element position and AOA distribution. We focus on the single side spatial correlation matrix $\mathbf{R}_{rx}$ at the Rx by assuming that i.i.d. array elements are equipped at the Tx. Our analysis is conducted by adopting a generic array model that can accommodate any 3D AOA distribution [19] with arbitrary positioning of antenna array elements [10]. For illustration, Fig. 1 shows the AOAs (θ, ϕ) of multipath components impinging on the Rx antenna array in a 3D (X', Y', Z') coordinate system, in which, the origin is the phase reference point. Let the m-th element of an antenna array be located at (x_m, y_m, z_m) and the corresponding position vector defined as $\mathbf{r}_m = (x_m, y_m, z_m)^T$. Based on Fig. 1, the wave vector is expressed by [42]

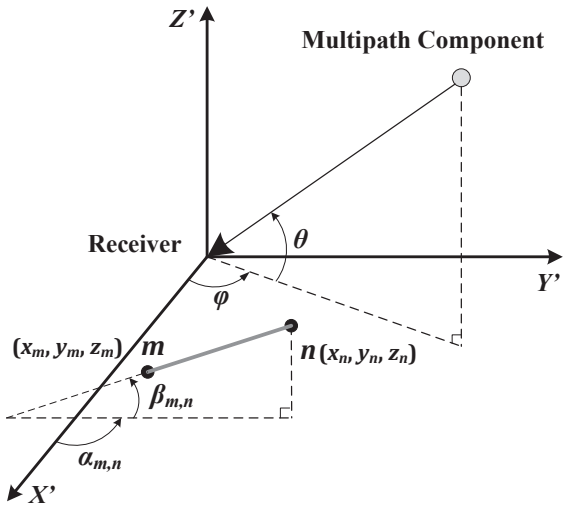

Fig. 1. Incident multipath component on two arbitrarily-located antenna array elements in 3D space.

$$\mathbf{k}(\theta, \phi) = \frac{2\pi}{\lambda}\begin{bmatrix}\cos(\theta)\cos(\phi)\\ \cos(\theta)\sin(\phi)\\ \sin(\theta)\end{bmatrix}. \tag{4}$$

The phase delay of a multipath component with AOAs (θ, ϕ) impinging onto the m-th element, i.e., the m-th input of the steering vector, is given by [42]

$$\begin{aligned} v_m(\theta, \phi) = \exp\{-j[\mathbf{r}_m \cdot \mathbf{k}(\theta, \phi)]\} = \exp\{-j(2\pi/\lambda) \\ [x_m\cos(\theta)\cos(\phi) + y_m\cos(\theta)\sin(\phi) + z_m\sin(\theta)]\} \end{aligned} \tag{5}$$

where $j = \sqrt{-1}$, and "$\cdot$" denotes the inner product. Since the spatial correlation between the m-th and the n-th array elements is the expectation of their phase difference (see eqs. (5), (12)) [12], the calculation incurs the position difference vector that can be evaluated by (see Fig. 1)

$$\begin{aligned} \mathbf{d}_{m,n} &= \mathbf{r}_n - \mathbf{r}_m \\ &= \begin{bmatrix}x_n\\ y_n\\ z_n\end{bmatrix} - \begin{bmatrix}x_m\\ y_m\\ z_m\end{bmatrix} = \begin{bmatrix}r_{m,n}\cos(\beta_{m,n})\cos(\alpha_{m,n})\\ r_{m,n}\cos(\beta_{m,n})\sin(\alpha_{m,n})\\ r_{m,n}\sin(\beta_{m,n})\end{bmatrix} \end{aligned} \tag{6}$$

where $r_{m,n} = \sqrt{(x_n - x_m)^2 + (y_n - y_m)^2 + (z_n - z_m)^2}$, $\beta_{m,n}$ denotes the angle between the $X'Y'$-plane and $\mathbf{d}_{m,n}$, and $\alpha_{m,n}$ is the angle between the X'-axis and the orthogonal projection of $\mathbf{d}_{m,n}$ on the $X'Y'$-plane.

C. Wireless Propagation Scenarios

We classify wireless propagation scenarios into three categories, namely, 3D isotropic, 3D directional and 3D omnidi-

rectional scenarios. Such classification accommodates any potential propagation scenario and modeling takes place through their specific AOA characteristics. In this paper, we will consider uniform and Gaussian AOA distributions as sufficient models for each propagation scenario, also due to their wide adoption in the published literature [9], [19]–[22]. In accordance with eq. (2) above, such scenarios account for diffuse (rich) multipath scattering.

1) 3D Directional Scenarios: In 3D directional propagation scenarios, we consider both restricted uniform and Gaussian distributions for the azimuth and elevation AOAs. Restricted uniform AOAs can heuristically model directional propagation and can be easily generalized to multi-clustered propagation [19]. Gaussian AOAs constitute a widely adopted and realistic modeling approach for directional propagation scenarios due to the concentricity of the Gaussian distribution [21].

Considering that the elevation and azimuth AOAs are independent to each other, the joint AOA distribution $P(\theta,\phi)$ can be written as $P(\theta,\phi) = P(\theta)P(\phi)$, where $P(\theta)$ and $P(\phi)$ are the marginal distributions for the elevation and azimuth AOAs, respectively [19]. Hence, the joint AOA distribution for 3D restricted uniform scenarios is expressed as [11]

$$P_u(\theta,\phi) = P_u(\theta)P_u(\phi) = 1/(4\Delta\phi\cos\theta_0\sin\Delta\theta) \quad (7)$$

where $\theta \in [\theta_0-\Delta\theta,\theta_0+\Delta\theta] \subseteq [-\pi/2,\pi/2]$, $\phi \in [\phi_0-\Delta\phi,\phi_0+\Delta\phi] \subseteq [-\pi,\pi]$, $P_u(\theta) = 1/(2\cos\theta_0\sin\Delta\theta)$ and $P_u(\phi) = 1/(2\Delta\phi)$ are the marginal uniform distributions for elevation and azimuth AOAs, θ_0 and ϕ_0 denote the mean elevation and azimuth AOAs, $\Delta\theta$ and $\Delta\phi$ determine the range of scattering sectors in elevation and azimuth, respectively. Note that by definition $\int_\theta P_u(\theta)\cos\theta d\theta = 1$, $\int_\phi P_u(\phi)d\phi = 1$.

The joint AOA distribution for 3D Gaussian scenarios, with $\theta \in [-\pi/2,\pi/2]$, $\phi \in [-\pi/2+\phi_0,\pi/2+\phi_0]$, can be expressed as [21]

$$\begin{aligned} P_{Gau}(\theta,\phi) &= P_{Gau}(\theta)P_{Gau}(\phi) \\ &= \frac{A_1}{\sqrt{2\pi}\sigma_\theta}\exp\left[-\frac{(\theta-\theta_0)^2}{2\sigma_\theta^2}\right]\frac{A_2}{\sqrt{2\pi}\sigma_\phi}\exp\left[-\frac{(\phi-\phi_0)^2}{2\sigma_\phi^2}\right] \end{aligned} \quad (8)$$

where $P_{Gau}(\theta)$, $P_{Gau}(\phi)$ are the marginal Gaussian distributions for the elevation and azimuth AOAs, respectively, and σ_θ, σ_ϕ are parameters related to the variance of each AOA distribution. In (8), A_1 and A_2 are normalization factors [22] such that by definition $\int_\theta P_{Gau}(\theta)\cos\theta d\theta = 1$, $\int_\phi P_{Gau}(\phi)d\phi = 1$.

2) 3D Isotropic Scenario: As an ideal case, the 3D isotropic scattering scenario can be modeled by the 3D restricted uniform scenario. The joint distribution for the 3D isotropic scenario arises from (7) by defining $\Delta\theta = \pi/2$, $\Delta\phi = \pi$, $\theta_0 = 0$, having

$$P_u(\theta,\phi) = 1/(4\pi). \quad (9)$$

3) 3D Omnidirectional Scenarios: In omnidirectional propagation scenarios, multipath power is uniformly distributed on the azimuth plane and directionally on elevation [20], [22]. It naturally lies between the directional and isotropic scenarios, completing wireless propagation classification. The azimuth AOA distribution is the uniform one, i.e., $P_u(\phi) = 1/(2\pi)$. We consider two cases for the elevation AOA in this paper, i.e., a restricted uniform and a Gaussian elevation AOA.

The joint distribution for the scenario with restricted uniform elevation AOA will be derived from (7) by defining $\Delta\phi = \pi$ as

$$P_{omni\_1}(\theta,\phi) = \frac{1}{4\pi\cos\theta_0\sin\Delta\theta}. \quad (10)$$

The joint distribution for the omnidirectional scenario with Gaussian elevation AOA can be derived from (8) by considering a uniform azimuth AOA i.e., $P_u(\phi) = 1/(2\pi)$, as follows [20]

$$\begin{aligned} P_{omni\_2}(\theta,\phi) &= P_{Gau}(\theta)P_u(\phi) \\ &= \frac{A_1}{2\pi\sqrt{2\pi}\sigma_\theta}\exp\left[-\frac{(\theta-\theta_0)^2}{2\sigma_\theta^2}\right]. \end{aligned} \quad (11)$$

III. Derivation of Closed-form Spatial Correlation Functions

The spatial correlation between the m-th and the n-th array elements is given by [9]

$$\begin{aligned} R_s(m,n) &= E\left\{v_m(\theta,\phi)v_n(\theta,\phi)^*\right\} \\ &= \int_\theta\int_\phi v_m(\theta,\phi)v_n(\theta,\phi)^*P(\theta,\phi)\cos(\theta)d\phi d\theta \end{aligned} \quad (12)$$

where $(.)^*$ denotes the conjugate transpose with $P(\theta,\phi)$ being the joint AOA distribution defined previously. To avoid the complicated numerical integrations in (12), we will use the JAE- and GHQ-based approximations to derive closed-form SCFs for antenna array topologies in 3D restricted uniform, Gaussian, and omnidirectional scenarios. The validity of the closed-form SCFs will be demonstrated in Section VI.

A. SCF for 3D Restricted Uniform Scenarios

For antenna arrays in 3D restricted uniform scenarios, we use (7) for $P(\theta,\phi)$ in eq. (12). A JAE-based approximation [10] is applied in this paper to derive the closed-form SCF (see Appendix A). Based on our system model as in Fig. 1, the closed-form SCF for arbitrary numbers and positions of array elements in 3D restricted uniform scenarios is expressed as

$$\begin{aligned} R_s(m,n) \approx{}& \frac{1}{Q\cos(\theta_0)\mathrm{sinc}(\Delta\theta)}\times \\ &\{[0.5f_0(\Theta_0)+f_0(\Theta_1)+...+f_0(\Theta_{Q-1})+0.5f_0(\Theta_Q)]+ \\ &2\sum_{g=1}^{G}(j^g\cos[g(\phi_0-\alpha_{m,n})]\mathrm{sinc}(g\Delta\phi)\times \\ &[0.5f_g(\Theta_0)+f_g(\Theta_1)+...+f_g(\Theta_{Q-1})+0.5f_g(\Theta_Q)])\} \end{aligned} \quad (13)$$

where $f_0(\Theta)$ and $f_g(\Theta)$ are defined in Appendix A, Θ_Q denotes the Q-th partition of the interval $[\theta_0-\Delta\theta,\theta_0+\Delta\theta]$ based on the Trapezoidal rule, and G is the summation term of JAE.

For antenna arrays in the 3D isotropic scenario, i.e., $P_u(\theta,\phi) = 1/(4\pi)$, the SCF can be analytically determined as [12]

$$R_s(m,n) = \mathrm{sinc}(2\pi r_{m,n}/\lambda). \quad (14)$$

B. SCF for 3D Gaussian Scenarios

For antenna arrays in 3D Gaussian scenarios, we use (8) for $P(\theta,\phi)$ in eq. (12) and apply a GHQ-based approximation approach to compute the double integrals of (12). The formula of GHQ rule can be found in [43] and expressed as

$$\int_{-\infty}^{\infty} e^{-x^2} f(x)dx = \sum_{b=1}^{B} \omega_b f(x_b) \tag{15}$$

where x_b, $b = 1, 2, ..., B$, are the zeros of the B-th order Hermite polynomial $H_B(x)$. The associated weight ω_b is given by [43]

$$\omega_b = \frac{2^{B-1}B!\sqrt{\pi}}{B^2[H_{B-1}(x_b)]^2}. \tag{16}$$

Employing the GHQ-based approximation approach as in [14], a novel closed-form SCF for arbitrary numbers and positions of antenna array elements in 3D Gaussian scenarios is derived in Appendix B as follows

$$\begin{aligned} &R_s(m,n) \approx \\ &\frac{A}{\pi}\sum_{q=1}^{M}\Bigg\{\omega_q \exp\left[j\frac{2\pi}{\lambda}r_{m,n}\sin(\sqrt{2}\sigma_\theta x_q+\theta_0)\sin(\beta_{m,n})\right] \\ &\times \cos(\sqrt{2}\sigma_\theta x_q+\theta_0) \\ &\times \sum_{p=1}^{N}\Bigg(\omega_p \exp\Bigg[j\frac{2\pi}{\lambda}r_{m,n}\cos(\beta_{m,n})\cos(\sqrt{2}\sigma_\theta x_q+\theta_0) \\ &\times \cos(\alpha_{m,n}-\sqrt{2}\sigma_\phi x_p-\phi_0)\Bigg]\Bigg)\Bigg\} \end{aligned} \tag{17}$$

where $A = A_1 \times A_2$, and M, N are the summation terms of Hermite polynomials. The abscissas x_p, $p = 1, 2, ..., N$, are the zeros of the N-th order Hermite polynomial, and x_q, $q = 1, 2, ..., M$, are the zeros of the M-th order Hermite polynomial, respectively.

Considering $P_{Gau}(\theta) = \delta(\theta)$ in (8) [20] and substituting $\beta_{m,n} = 0$ and $\sqrt{2}\sigma_\theta x_q + \theta_0 = 0$ into (17) yields the SCF for 2D arrays in 2D Gaussian scenarios as was derived in [14, eq. (15)].

C. SCF for 3D Omnidirectional Scenarios

For antenna arrays in 3D omnidirectional scenarios with restricted uniform elevation AOA, we use (10) for $P(\theta,\phi)$ in eq. (12). The SCF in (13) still holds by defining $\Delta\phi = \pi$. For antenna arrays in the omnidirectional scenario with Gaussian elevation AOA, we use (11) for $P(\theta,\phi)$ in eq. (12). Combining the JAE and GHQ approaches, the closed-form SCF in this scenario is derived in Appendix C as follows

$$\begin{aligned} R_s(m,n) \approx \frac{A_1}{\sqrt{\pi}}\sum_{q=1}^{M}\Bigg\{&\omega_q \exp\Big[j2\pi r_{m,n}\sin(\sqrt{2}\sigma_\theta x_q+\theta_0) \\ &\times \sin(\beta_{m,n})/\lambda]\cos(\sqrt{2}\sigma_\theta x_q+\theta_0) \\ &\times J_0\left(j2\pi r_{m,n}\cos(\sqrt{2}\sigma_\theta x_q+\theta_0)\cos(\beta_{m,n})/\lambda\right)\Bigg\}. \end{aligned} \tag{18}$$

IV. Spatial Degrees of Freedom Analysis

The DoF, being the product of the AOA solid angle range, i.e, the SDoF, and array aperture size, determine the maximum number of antenna array elements to be employed at a single side, i.e., the Rx, for optimum channel capacity [15]. Inversely, with given numbers of elements, knowledge of SDoF is sufficient to determine the minimum occupied space for antenna arrays and this will be demonstrated in Section VI. The SDoF outcome in [15] is actually valid for uniform AOA distributions, i.e., when assigning a uniform AOA distribution in the designated AOA range. We will generalize such SDoF outcome by extending it to any AOA distribution. Correctness will be confirmed in Section VI by demonstrating performance compliance of different AOA scenarios with equal DoF.

A. SDoF Formulas [15]

For a linear array with $2L$ (in λ) length placed along the $Z^{'}$-axis and centered at the origin, the DoF can be evaluated by

$$X = 2L\left|\Omega_\theta\right| + 1 \tag{19}$$

where $|\Omega_\theta|$ denotes the range of $\cos\theta$ and can be expressed as

$$\left|\Omega_\theta\right| = \int_{\theta_0-\Delta\theta}^{\theta_0+\Delta\theta} \cos\theta d\theta = 2\cos\theta_0 \sin\Delta\theta. \tag{20}$$

For a circular array located on the $X^{'}Y^{'}$-plane and centered at the origin with radius R (in λ), the DoF can be expressed as

$$X = 2R\left|\Phi\right| \tag{21}$$

in which $|\Phi|$ is the range of ϕ and expressed as

$$\left|\Phi\right| = \int_{\phi_0-\Delta\phi}^{\phi_0+\Delta\phi} d\phi = 2\Delta\phi. \tag{22}$$

Compared with linear and circular arrays, spherical arrays capture all SDoF of the 3D spatial propagation channel and thus provide higher capacity. For a spherical array centered at the origin with radius R (in λ), the DoF is

$$X = \pi R^2\left|\Omega\right| \tag{23}$$

where $|\Omega|$ is the range of Ω denoting the SDoF. An alternative interpretation of $|\Omega|$ is that it denotes the DoF captured by a spherical array of unit aperture πR^2, i.e., the SDoF are the DoF per unit array aperture. Thus, if we know $|\Omega|$ as the spatial resolution of the propagation channel and we wish to use X antenna elements, we can alternatively calculate the required radius R of the spherical array to accommodate these X elements for optimum channel capacity. Therefore, for spherical arrays, the SDoF when Ω occupies a single scattering sector will be the product of (20) and (22) as

$$\left|\Omega\right| = \left|\Omega_\theta\right|\left|\Phi\right| = \int_\theta\int_\phi \cos\theta d\phi d\theta = 4\Delta\phi\cos\theta_0\sin\Delta\theta. \tag{24}$$

B. Generalized SDoF Formulas

We heuristically derive generalized SDoF formulas applicable to any AOA distribution, without just considering the range of Ω as in [15]. This is done with the aid of the differential entropy and the validity of our heuristic formulations will be demonstrated in Section VI. The proposed formulation can be adaptable to any wireless propagation scenario characterized by its AOA distribution.

In information theory, the differential entropy $H(Y)$ of a continuous random variable Y shows the uncertainty of the variable, i.e., the amount of information contained in the variable, and is defined as [36]

$$H(Y) = -\int_S P(y)\log_2 P(y)dy \tag{25}$$

where $P(y)$ is the distribution of Y, S is the support set of the random variable Y, and the volume of S is expressed as $2^{H(Y)}$. In fact, $2^{H(Y)}$ characterizes the independent dimensions, i.e., the DoF, subtended by the random variable Y with distribution $P(y)$. We apply this concept to find the SDoF subtended by the AOA distribution in the 3D space. Considering the AOA distribution $P(\Omega)$ with respect to the solid angle Ω, we can define the differential entropy of the AOA distribution similarly to (25) as $H(\Omega) = -\int_\Omega P(\Omega)\log_2 P(\Omega)d\Omega$. Based on the theorem of the change of variable [44, Appendix B], under the mapping $\Omega \to \theta, \phi$, with $P(\Omega)d\Omega = \cos\theta P(\theta,\phi)d\phi d\theta$, the differential entropy of the joint AOA distribution can be expressed as

$$H(\theta,\phi) = -\int_\theta\int_\phi \cos\theta P(\theta,\phi)\log_2 P(\theta,\phi)d\phi d\theta. \tag{26}$$

We can thus heuristically determine the SDoF as $|\Omega| = 2^{H(\theta,\phi)}$ for any AOA distribution.

For the restricted uniform AOA, the SDoF for spherical arrays are derived in Appendix D as

$$|\Omega| = 2^{H_u(\theta,\phi)} = 4\Delta\phi\cos\theta_0\sin\Delta\theta \tag{27}$$

which coincides with (24). Thus, just considering the AOA range as in [15] is equivalent to assigning a restricted uniform distribution within that AOA range. If the propagation channel contains more than one scattering region, i.e., multi-clustered wireless propagation (see [19]), then $|\Omega|$ will arise by summing contributions similar to (27) for each scattering region. The SDoF for linear and circular arrays are given by (see Appendix D)

$$|\Omega_\theta| = 2^{H_u(\theta)} = 2\cos\theta_0\sin\Delta\theta \tag{28}$$

$$|\Phi| = 2^{H_u(\phi)} = 2\Delta\phi \tag{29}$$

respectively. (28) and (29) are identical to (20) and (22), respectively. From (27), the SDoF for the 3D isotropic propagation scenario, i.e., $\theta_0 = 0$, $\Delta\theta = \pi/2$, $\Delta\phi = \pi$, becomes $|\Omega| = 4\pi$, equal to the full range of solid angle in the 3D space.

Using (26) in 3D Gaussian scenarios, the SDoF for spherical arrays can be heuristically determined as (see Appendix D)

$$|\Omega|_{Gau} = 2^{H_{Gau}(\theta,\phi)} = \frac{2\pi\sigma_\theta\sigma_\phi}{A_1A_2}\exp\left\{\frac{\sigma_\phi^2 V_{Gau}(\theta)+\sigma_\theta^2 V_{Gau}(\phi)}{2\sigma_\theta^2\sigma_\phi^2}\right\} \tag{30}$$

where $V_{Gau}(\theta)$ and $V_{Gau}(\phi)$ are the variances of θ and ϕ, respectively, defined as

$$V_{Gau}(\theta) = \int_\theta (\theta-\theta_0)^2 P_{Gau}(\theta)\cos\theta d\theta \tag{31}$$

$$V_{Gau}(\phi) = \int_\phi (\phi-\phi_0)^2 P_{Gau}(\phi)d\phi. \tag{32}$$

The SDoF for linear and circular arrays in 3D Gaussian scenarios are given by

$$|\Omega_\theta|_{Gau} = 2^{H_{Gau}(\theta)} = \frac{\sqrt{2\pi}\sigma_\theta}{A_1}\exp\left[\frac{V_{Gau}(\theta)}{2\sigma_\theta^2}\right] \tag{33}$$

$$|\Phi|_{Gau} = 2^{H_{Gau}(\phi)} = \frac{\sqrt{2\pi}\sigma_\phi}{A_2}\exp\left[\frac{V_{Gau}(\phi)}{2\sigma_\phi^2}\right] \tag{34}$$

respectively (see Appendix D). Such results are brand-new, extending [15], and the whole analysis can be applied to any AOA distribution. Validity will be demonstrated in Section VI.

In 3D omnidirectional scenarios for the cases of uniform and Gaussian elevation AOA, the SDoF for spherical arrays can be heuristically determined as

$$|\Omega|_{omni\_1} = |\Omega_\theta|\,|\Phi| = 4\pi\cos\theta_0\sin\Delta\theta \tag{35}$$

$$|\Omega|_{omni\_2} = |\Omega_\theta|_{Gau}\,|\Phi| = \frac{2\pi\sqrt{2\pi}\sigma_\theta}{A_1}\exp\left[\frac{V_{Gau}(\theta)}{2\sigma_\theta^2}\right] \tag{36}$$

respectively, where we used (28), (33), and $|\Phi| = 2\pi$, as the azimuth AOA is uniformly distributed in $[-\pi,\pi]$.

V. PSOvm Algorithm Implementation

A. PSOvm Fundamentals

We present the implementation of PSOvm in finding optimum antenna array topologies with maximum MIMO capacities. Basic theory of PSO has been comprehensively presented in [45]. The descriptive terms of PSO can be found in [45, Table I] and the updates of velocity v_i and position x_i for the i-th ($i = 1, 2, ..., n$) particle at each moment t ($t = 0, 1, 2, ..., T$) are given by

$$\begin{aligned} &v_i(t+1) = \\ &k\left\{\omega v_i(t) + c_1 r_1[p_i(t) - x_i(t)] + c_2 r_2[g(t) - x_i(t)]\right\} \end{aligned} \tag{37}$$

$$x_i(t+1) = x_i(t) + v_i(t+1) \tag{38}$$

where k is the constriction factor, $p_i(t)$ and $g(t)$ are the personal best (pbest) and the global best (gbest) position found by the i-th particle and the swarm at moment t, respectively. c_1 and c_2 are acceleration coefficients, r_1 and r_2 are random numbers in $(0, 1)$. To keep particles unaffected from pulling of pbest and gbest results, the inertial weight $\omega \sim (0, 1)$ is linearly decreased from $c_{start} = 0.9$ to $c_{end} = 0.4$ as [45]

$$\omega = c_{start} - \left[\frac{c_{start} - c_{end}}{T}\right] \times t. \tag{39}$$

However, the recent study [30] proposed a PSOvm technique that outperforms the classic PSO as it helps to improve the particles' positions at the first few iterations for a better

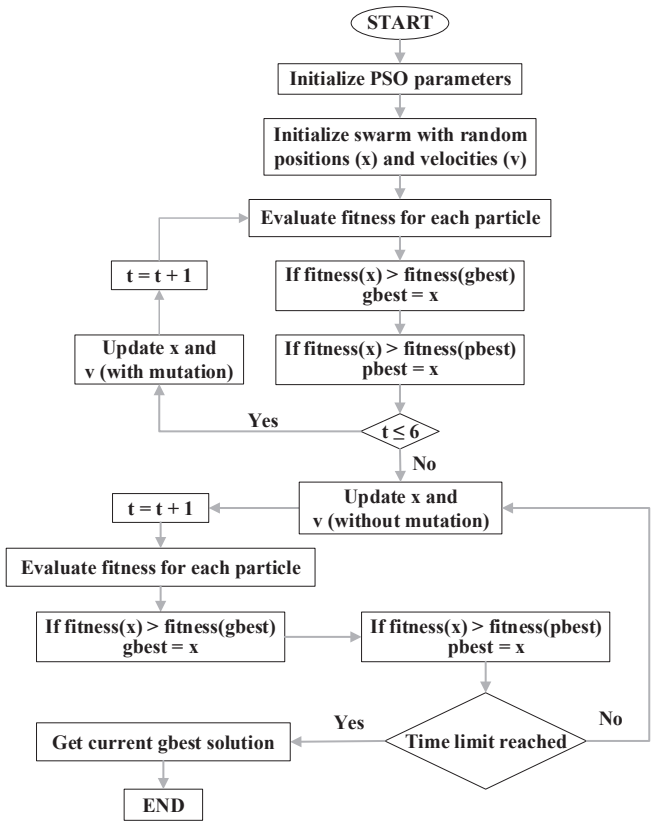

Fig. 2. PSOvm algorithm flowchart.

fitness, and thus improves the overall algorithm performance. Its velocity update can be developed from (37) as

$$v_i(t+1) = \\ k\left\{F_l v_i(t) + c_1 r_1[p_i(t) - x_i(t)] + c_2 r_2[g(t) - x_i(t)]\right\} \tag{40}$$

where F_l is the mutation factor given by [30]

$$F_l = (0.1l + 0.6)(2r - 1), \qquad l = 1, ..., 6 \tag{41}$$

where r is a random number in $(0, 1)$. We will use (40) and (41) in the beginning to update the velocity for six times, for the purpose of acceptable convergence speed as was verified in [30]. The remaining velocity updates will carry on with (37). The position updates will follow (38) for the whole searching. Before starting the optimization, we define the searching space as

$$\sqrt{x_{mo}^2 + y_{mo}^2 + z_{mo}^2} \leq D_{max} \tag{42}$$

where D_{max} denotes the radius of a spherical searching space centered at the origin and (x_{mo}, y_{mo}, z_{mo}) is the obtained optimum position of the m-th antenna array element. Based on the PSOvm flowchart as plotted in Fig. 2, the maximization of ergodic MIMO channel capacity (fitness) in (3) by finding optimum positions of antenna array elements in a constrained space is summarized step-by-step in the following sub-section.

B. Optimization Process

1) *Initialization of Particles and Swarms:* We set the particle number to $n = 20$ as the study in [46] demonstrated that 20 particles are effective enough for most engineering problems, and the time limit to $T = 500$ being large enough for a reasonable computation time [10]. The work in [47] found that v_{max} is best set to $10\% - 20\%$ of the width of searching space, we thus select the median one as $v_{max} = 0.15 D_{max}$. We select the standard choice $k = 0.73$ as was suggested in [45], and the optimal choices $c_1 = 2.8$, $c_2 = 1.3$ as were validated in [46].
2) *Initialization of Algorithm:* We randomly locate the initial pbest position $p_i(1)$ of the i-th particle and the initial gbest position $g(1)$ of the swarm in the searching space, $i = 1, 2, ..., 20$, such that none of the particles know where the gbest position is located yet. The initial velocity $v_i(1)$, $i = 1, 2, ..., 20$ is random in both its direction and magnitude. Both the initial pbest fitness $C_{pbest}(i)$ for the i-th particle and the initial gbest fitness C_{gbest} for the swarm are set to zero to realize the correct capacity in the following searching process.
3) *Fitness Evaluation:* At each moment t, $t = 0, 1, 2, ..., 500$, each particle randomly flies through the searching space and computes the fitness at their positions $x_i(t)$, $i = 1, 2, ..., 20$. Comparing the obtained fitness C with the pbest fitness $C_{pbest}(i)$, if $C > C_{pbest}(i)$, replace $C_{pbest}(i)$ with the current C and $p_i(t)$ with the current position $x_i(t)$. Similarly, comparing C with the gbest fitness C_{gbest}, set C_{gbest} to C and $g(t)$ to $x_i(t)$ if $C > C_{gbest}$.
4) Update the mutated velocity v_i with (40), (41) and the position x_i with (38) for each particle. Any of the particles flying beyond the searching space will be hauled back to the boundary when the condition in (42) is applied.
5) Set $t = t + 1$, and repeat the process in 3) and 4) if $t \leq 6$. Otherwise, move to the next step.
6) Update the velocity v_i with (37) and the position x_i with (38) for each particle. The condition in (42) is still applied.
7) Set $t = t + 1$, repeat the process in 3) and carry on the position and velocity updating with 6) if $t \leq 500$. Otherwise, terminate the optimization process.

VI. Simulations and Results

In this section, we demonstrate and verify the validity of our methodology in realizing optimum antenna array topologies with maximum capacity performance occupying minimum space. Simulations and results for the wireless propagation scenarios discussed in Section II-C are comprehensively presented. Empowered by the existence of analytical SDoF formulas in Section IV, we focus on linear, circular, and spherical array topologies.

Based on the wireless propagation scenarios discussed in Section II-C, the AOA parameters for each of the scenarios are defined and listed in Table I. For the 3D restricted uniform scenario (see (7)), we assume $\theta_0 = \phi_0 = 0$, $\Delta\theta = \Delta\phi = \pi/6$. The variances for the uniform elevation and azimuth AOAs,

TABLE I
AOA PARAMETERS IN EACH PROPAGATION SCENARIO

3D Propagation Scenario	Elevation AOA	Azimuth AOA
Isotropic	$\theta \sim U[-\pi/2, \pi/2]$, $\theta_0 = 0, \Delta\theta = \pi/2$	$\phi \sim U[-\pi, \pi]$, $\phi_0 = 0, \Delta\phi = \pi$
Restricted uniform	$\theta \sim U[-\pi/6, \pi/6]$, $\theta_0 = 0, \Delta\theta = \pi/6$	$\phi \sim U[-\pi/6, \pi/6]$, $\phi_0 = 0, \Delta\phi = \pi/6$
Gaussian (variance)	$\theta \in N(\theta_0, \sigma_\theta^2)$, $\theta_0 = 0, \sigma_\theta = 0.3123$	$\phi \in N(\phi_0, \sigma_\phi^2)$, $\phi_0 = 0, \sigma_\phi = 0.3023$
Gaussian (entropy)	$\theta \in N(\theta_0, \sigma_\theta^2)$, $\theta_0 = 0, \sigma_\theta = 0.2588$	$\phi \in N(\phi_0, \sigma_\phi^2)$, $\phi_0 = 0, \sigma_\phi = 0.2533$
Omnidirectional-1	$\theta \sim U[-\pi/6, \pi/6]$, $\theta_0 = 0, \Delta\theta = \pi/6$	$\phi \sim U[-\pi, \pi]$, $\phi_0 = 0, \Delta\phi = \pi$
Omnidirectional-2	$\theta \in N(\theta_0, \sigma_\theta^2)$, $\theta_0 = 0, \sigma_\theta = 0.3123$	$\phi \sim U[-\pi, \pi]$, $\phi_0 = 0, \Delta\phi = \pi$

$V_u(\theta)$ and $V_u(\phi)$, respectively, are determined as

$$V_u(\theta) = \int_{\theta_0-\Delta\theta}^{\theta_0+\Delta\theta} (\theta-\theta_0)^2 P_u(\theta)\cos\theta d\theta = \Delta\theta^2 + \frac{2\Delta\theta\cos\Delta\theta}{\sin\Delta\theta} - 2 \tag{43}$$

$$V_u(\phi) = \int_{\phi_0-\Delta\phi}^{\phi_0+\Delta\phi} (\phi-\phi_0)^2 P_u(\phi) d\phi = \frac{\Delta\phi^2}{3} \tag{44}$$

where, (43) arises by using the definition for $P_u(\theta)$ (see below eq. (7)) and after some algebraic manipulations with the aid of [48, eqs. 2633-5, 6]. By using the definition for $P_u(\phi)$ (see below eq. (7)) and after some elementary algebraic manipulations, (44) arises. For 3D isotropic scenarios, we just assign $\theta_0 = \phi_0 = 0$, $\Delta\theta = \pi/2$, $\Delta\phi = \pi$ (see (9)).

For fair comparison between 3D restricted uniform and 3D Gaussian scenarios, we assume $\theta_0 = \phi_0 = 0$, and σ_θ, σ_ϕ to be defined via two different ways, i.e., equating the variances or the differential entropies of both distributions. First, we can consider the Gaussian variances of (31) and (32) being equal to the uniform variances of (43) and (44), respectively. Then, we use (8) to solve both equations numerically resulting in $\sigma_\theta = 0.3123$, $\sigma_\phi = 0.3023$. Besides that, we can define σ_θ and σ_ϕ by equating the Gaussian entropies of (33) and (34) to the uniform entropies of (28) and (29), respectively. Then, we use (8), (31) and (32) to solve both equations numerically resulting in $\sigma_\theta = 0.2588$, $\sigma_\phi = 0.2533$. The notes of 'variance' and 'entropy' in figures and tables refer to the 3D Gaussian scenarios by determining σ_θ, σ_ϕ via these two different ways.

For the 3D omnidirectional scenario $P_{omni\_1}(\theta, \phi)$ with restricted uniform elevation AOA (see (10)), the angular parameters are defined as $\theta_0 = \phi_0 = 0$, $\Delta\theta = \pi/6$, $\Delta\phi = \pi$. For the 3D omnidirectional scenario $P_{omni\_2}(\theta, \phi)$ with Gaussian elevation AOA (see (11)), the angular parameters are defined as $\theta_0 = \phi_0 = 0$, $\sigma_\theta = 0.3123$, $\Delta\phi = \pi$.

We calculate the ergodic capacity by averaging over $3,000$ realizations of MIMO channels. All distances/lengths are normalized by λ. We set the SNR $P/\sigma_n^2 = 10$ dB as in [15], being sufficiently high in order the ergodic MIMO channel capacity to be DoF limited rather than power limited [6]. As was verified in [14], JAE and GHQ have similar approximation performance when $G = 20$ (see (13)), $M = N = 10$ (see (17)), respectively. However, to achieve an approximation accuracy up to six decimal places when comparing the closed-form SCF with its respective numerical computation, we select $G = 50$ in (13) for the JAE in all scenarios. For GHQ, we increase the terms of M, N in (17), (18) from 20 (for 2×2 MIMO) to 140 (for 35×35 MIMO) for a similar approximation performance compared with the JAE. The number of the Trapezoidal subintervals in (13) is set to $Q = 1000$. In this paper, we only consider the correlation at the Rx side in MIMO systems ($N_r = N_t$) applying the Kronecker model, i.e., the Tx antennas are assumed to be separated sufficiently apart such that $\mathbf{R}_{tx} = \mathbf{I}_{N_t}$. However, the adopted methodology can be readily extended to account for correlation at both sides leveraging the uncoupled correlation formulation of the MIMO Kronecker model. The theoretical i.i.d. capacity is obtained by assuming $\mathbf{R}_{tx} = \mathbf{I}_{N_t}$, $\mathbf{R}_{rx} = \mathbf{I}_{N_r}$ and using (2), (3).

A. Validation of the Closed-Form SCFs of (13), (17), (18)

To verify the derived closed-form SCFs for each of the scenarios, comparisons with the numerical and theoretical SCFs in a 2×2 MIMO channel will be considered first. As the spatial correlation depends on the distance between two antenna elements (see (12)), considering a 2×2 case is sufficient for the verification of the closed-form solutions [9]. We assume that two Rx antennas are located at P1 $(-D/4, -D/4, \sqrt{2}D/4)$ and P2 $(D/4, D/4, -\sqrt{2}D/4)$, the spacing between them can thus be quantified by D. We use (13) to compute the spatial correlations for the 3D isotropic, restricted uniform, and omnidirectional scenario with restricted uniform elevation AOA, (17) for the two 3D Gaussian scenarios (variance and entropy), and (18) for the 3D omnidirectional scenario with Gaussian elevation AOA. The numerical SCFs calculated by the integrations of (12) for each of the scenarios and the analytical SCF of (14) for the 3D isotropic scenario will be included for comparisons. Fig. 3 depicts the absolute SCFs between elements $(1, 2)$ against the spacing D for the various 3D scenarios and the closed-form SCFs show excellent agreements with the numerical SCFs. Besides that, the closed-form SCF of (13) is identical to the analytical formula of (14) for the 3D isotropic scenario. Fig. 3 also shows that the SCFs of the two 3D omnidirectional scenarios lie between the 3D isotropic and 3D directional scenarios being very close to the 3D isotropic one. The results validate the 3D closed-form SCFs of (13), (17), and (18) derived in Section III adopting the JAE- and GHQ-based approximation techniques.

We also verify the PSOvm algorithm presented in Section V by comparing the achieved ergodic channel capacity with the theoretical maximum of the i.i.d. case in a 2×2 MIMO channel. Table II shows that in all AOA scenarios, the PSOvm finds the maximum ergodic MIMO channel capacity being equal to the theoretical maximum, assigning optimum Rx element spacing and consuming only a few iterations. Such optimum spacing leading to maximum ergodic MIMO channel capacity complies with the SCF behaviors depicted in Fig. 3, i.e., the optimum spacing derived in Table II complies with the spacing around the first zero of the respective SCF in Fig. 3. Such outcomes verify the adopted PSOvm technique and demonstrate its efficiency in solving the ergodic MIMO

TABLE II
PSOvm PERFORMANCE FOR 2×2 MIMO CAPACITY MAXIMIZATION IN EACH PROPAGATION SCENARIO

3D Propagation Scenario	Convergence at Iteration	Time consumption for each iteration (closed-form SCFs) (in s)	Time consumption for each iteration (closed-form SCFs) (in s)	Maximized Capacity (in bit/s/Hz)	Optimum Spacing (in λ)
Isotropic	9	6.9	137.5	5.5380	0.4952
Restricted uniform	12	8.0	150.1	5.5380	1.9549
Gaussian (variance)	7	5.7	3485.0	5.5380	1.8772
Gaussian (entropy)	7	6.6	5772.7	5.5380	1.7813
Omnidirectional-1	3	4.5	201.8	5.5380	0.4964
Omnidirectional-2	10	6.6	483.1	5.5380	0.4889

* For a 2×2 MIMO channel, the theoretical maximum ergodic capacity is 5.5380 bits/s/Hz.

TABLE III
PHYSICAL SPACE CONSTRAINTS OF STANDARDIZED ARRAY TOPOLOGIES IN EACH PROPAGATION SCENARIO

3D Propagation Scenario	Spatial DoF	Linear Array: $2L\,\lvert\Omega_\theta\rvert + 1 = 10$	Circular Array: $2R\,\lvert\Phi\rvert = 10$	Spherical Array: $\pi R^2\,\lvert\Omega\rvert = 10$
Isotropic	$\lvert\Omega_\theta\rvert = 2$ $\lvert\Phi\rvert = 2\pi$ $\lvert\Omega\rvert = 4\pi$	$L = 0.2500\lambda$	$R = 0.7958\lambda$	$R = 0.5033\lambda$
Restricted uniform	$\lvert\Omega_\theta\rvert = 1$ $\lvert\Phi\rvert = 1.0472$ $\lvert\Omega\rvert = 1.0472$	$L = 4.5000\lambda$	$R = 4.7746\lambda$	$R = 1.7435\lambda$
Gaussian (variance)	$\lvert\Omega_\theta\rvert_{Gau} = 1.1707$ $\lvert\Phi\rvert_{Gau} = 1.2493$ $\lvert\Omega\rvert_{Gau} = 1.4626$	$L = 3.8439\lambda$	$R = 4.0022\lambda$	$R = 1.4752\lambda$
Gaussian (entropy)	$\lvert\Omega_\theta\rvert_{Gau} = 1$ $\lvert\Phi\rvert_{Gau} = 1.0472$ $\lvert\Omega\rvert_{Gau} = 1.0472$	$L = 4.5000\lambda$	$R = 4.7746\lambda$	$R = 1.7435\lambda$
Omnidirectional-1	$\lvert\Omega_\theta\rvert = 1$ $\lvert\Phi\rvert = 2\pi$ $\lvert\Omega\rvert_{omni\_1} = 2\pi$			$R = 0.7118\lambda$
Omnidirectional-2	$\lvert\Omega_\theta\rvert_{Gau} = 1.1707$ $\lvert\Phi\rvert = 2\pi$ $\lvert\Omega\rvert_{omni\_2} = 7.3557$			$R = 0.6578\lambda$

* $2L$ denotes the length of linear arrays, R is the radius of circular and spherical arrays.

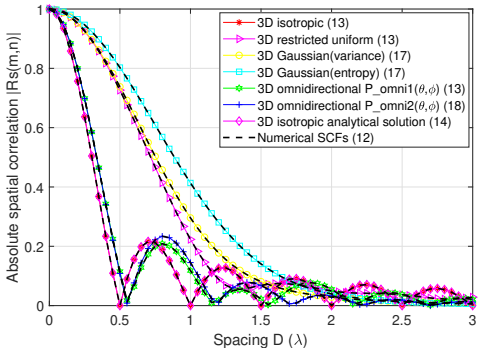

Fig. 3. SCF between two receive antennas in each propagation scenario.

channel capacity maximization problem. Note that the number of iterations required for convergence shows some variations in different AOA scenarios. This can be attributed to the random initial positions of particles finding the best solution near to where they were initially located. Another reason can be the different computational complexity of the closed-form SCF in each scenario. In all 3D propagation scenarios of Table II, the iteration time consumption with numerical SCF evaluation is considerably larger than the respective with closed-form SCF. Such observation further justifies the necessity of deriving closed-form SCFs. Once the closed-form SCFs and PSOvm are verified, we can proceed in verifying the SDoF formulations presented in Section IV.

B. Verification of the SDoF Formulations

To verify the SDoF formulations presented in Section IV, we will derive capacity performance with respect to the number of antenna array elements for linear, circular, and spherical topologies. Starting with the 3D restricted uniform scenario, we assume that the maximum antenna numbers in (19), (21) and (23) for linear, circular and spherical arrays are $X = 10$. Using (28), (29), (27) for the 3D restricted uniform scenario into the corresponding DoF formulas (19), (21), (23), the physical dimensions of linear, circular, and spherical arrays are obtained and listed in Table III. Allowing the PSO particles to search on the array boundaries only and running the algorithm, the maximized capacities along with the increasing numbers of array elements are plotted in Fig. 4. Fig. 4 shows that in the 3D restricted uniform scenario, when we have $X = 10$ elements in all array topologies, the ergodic MIMO channel capacity follows the i.i.d case and starts deviating after that value. Similar observations are reported for the 3D omnidirectional and isotropic scenarios. Such results, holding for 3D uniform AOA scenarios, interpret the DoF outcomes derived in [15].

Next, we consider 3D Gaussian scenarios to demonstrate the correctness of our heuristic SDoF formulations. We use the SDoF of (33), (34), (30) for the 3D Gaussian scenarios into the respective DoF formulas (19), (21), (23). The physical dimensions of linear, circular, and spherical arrays can be found in Table III. The maximized capacities versus antenna

This article has been accepted for publication in IEEE Transactions on Wireless Communications. This is the author's version which has not been fully edited and content may change prior to final publication. Citation information: DOI 10.1109/TWC.2022.3231732

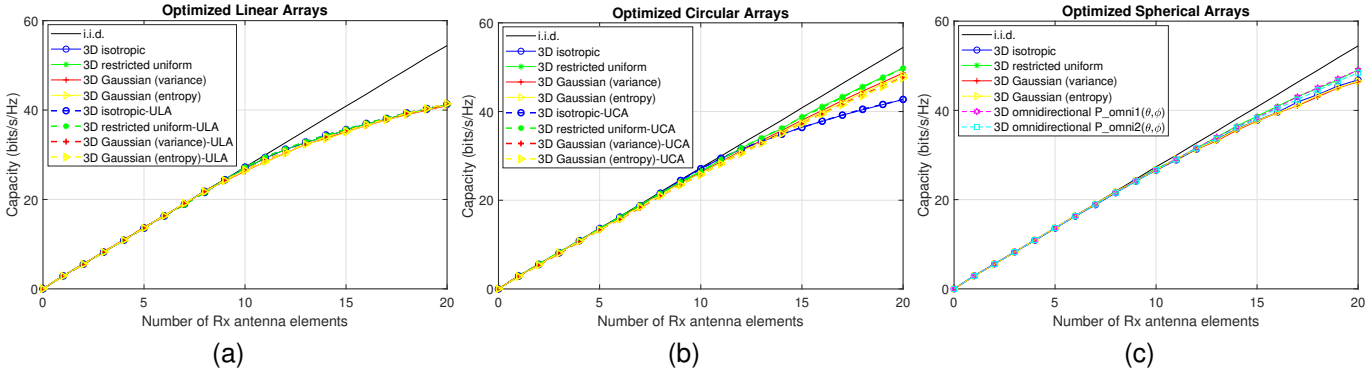

Fig. 4. Capacity versus number of array elements in each propagation scenario (with $X = 10$).

TABLE IV
MAXIMUM CAPACITIES IN EACH PROPAGATION SCENARIO

Array Geometry	3D Propagation Scenario	Max Capacity (bits/s/Hz)
Linear array	Isotropic	27.0349
	Restricted uniform	27.0160
	Gaussian (variance)	26.5174
Circular array	Isotropic	26.9439
	Restricted uniform	27.0003
	Gaussian (variance)	26.7187
Spherical array	Isotropic	26.5577
	Restricted uniform	26.9598
	Gaussian (variance)	26.6820
	Omnidirectional-1	26.6958
	Omnidirectional-2	26.5707
Arbitrarily-shaped 3D array	Isotropic	26.6615
	Restricted uniform	27.0035
	Gaussian (variance)	26.6233
	Omnidirectional-1	26.7212
	Omnidirectional-2	26.5412

* For a 10×10 MIMO channel, theoretical i.i.d. capacity is 27.0478 bits/s/Hz.

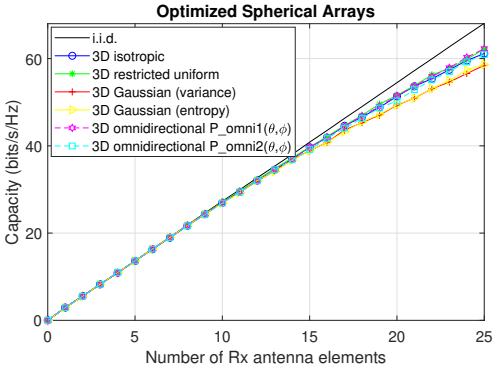

Fig. 5. Capacity versus number of array elements in each propagation scenario (with $X = 15$).

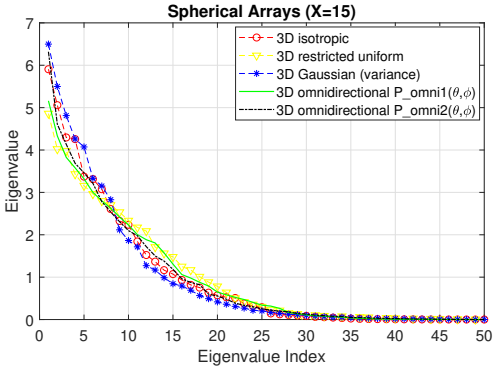

Fig. 6. Eigenvalues of the 50×50 $\mathbf{R}_{rx}$ in each propagation scenario.

numbers are plotted in Fig. 4. Again, packing more than $X = 10$ elements cannot achieve the i.i.d. capacity as shown in Fig. 4. It thus validates our heuristic SDoF formulations can be applied in any wireless propagation scenario, i.e., 3D Gaussian in this paper, having performance compliance with the (validated from [15]) 3D uniform ones. Additionally, Fig. 4 shows that the capacity performances of the Gaussian (variance) and Gaussian (entropy) cases are identical to each other, which confirms both methods in defining the Gaussian AOA parameters. Table III also demonstrates that antenna arrays occupy less space in the 3D Gaussian (variance) scenario compared with the 3D Gaussian (entropy) for achieving the same capacity performance. We will consider the 3D Gaussian (variance) scenario for the remainder of the paper.

In 3D omnidirectional scenarios, we will just consider 3D antenna array topologies, as capacity performance of linear and circular ones depends exclusively on the elevation and azimuth AOA distributions, respectively. But such analysis has been already conducted previously in the various directional and isotropic scenarios. Using (35) and (36) into (23), we derive the radius R of the spherical array topology space for each omnidirectional scenario (see Table III). The capacity behavior for both 3D omnidirectional scenarios in Fig. 4(c) demonstrates that $X = 10$ is the maximum number of elements to achieve the i.i.d. capacity.

In all propagation scenarios, we have also included the capacities for ULAs and UCAs in Figs. 4(a) and 4(b), respectively. Capacity performance of such standardized topologies is almost identical to the optimized ones in all scenarios. It is thus revealed that good antenna array design is possible by just knowing the SDoF, without running time and resource consuming optimizations. Results in Fig. 4 and Table III show that for linear increase in the ergodic MIMO channel capacity, the element number is indeed 10 in each array topology and all wireless propagation scenarios. Further insight into the results of Fig. 3 and Table III reveals the (rational) behavior that in similar scenarios classified either as 3D uniform or 3D

This article has been accepted for publication in IEEE Transactions on Wireless Communications. This is the author's version which has not been fully edited and content may change prior to final publication. Citation information: DOI 10.1109/TWC.2022.3231732

Gaussian, the greater the SDoF, the lower the SCFs are. More specifically, the 3D isotropic, omnidirectional-1, and restricted uniform AOA scenarios are classified in descending order in terms of SDoF, but in ascending order in terms of SCFs. Same applies for the 3D Gaussian (variance) and Gaussian (entropy) scenarios. In the 3D restricted uniform and 3D Gaussian (entropy) scenarios, their SCFs are not the same, although their SDoF are equal. This can be attributed to the chosen orientation of the two elements used to compute the SCFs shown in Fig. 3. In the following, we will focus on optimizing spherical arrays as they cannot demonstrate a sole uniform topology.

Furthermore, the ergodic MIMO channel capacity for $X = 15$ is presented in Fig. 5. Again, Fig. 5 demonstrates that for linear increase in the ergodic MIMO channel capacity the element number is 15 in spherical array topologies and all wireless propagation scenarios. Similar observations are reported in linear and circular cases. Note that, the required minimum spaces for $X = 15$ are different from the ones for $X = 10$ and can be determined by the SDoF in a similar way as was done in the $X = 10$ case. With such limitation of $X = 15$, we also evaluate the eigenvalues of $\mathbf{R}_{rx}$ considering a 50×50 spatial correlation matrix for different wireless propagation scenarios as depicted in Fig. 6. Fig. 6 reveals a similar eigenvalue behavior trend in all 3D AOA scenarios, with eigenvalues tending to zero after the value 15. As the eigenvalue behavior of the spatial correlation matrix constitutes another interpretation of the DoF according to [34], [35], such result further verifies our SDoF formulations. Apart from confirming the proposed SDoF formulations, such results can constitute a pathway for antenna array design given the propagation channel characteristics. More specifically, the critical factor for devising antenna arrays occupying minimum space is the AOA entropy and not the AOA distribution itself. Furthermore, should we just know the descriptive statistics (i.e., mean and variance) of the AOA distribution from a given wireless propagation channel measurement campaign, we can safely assume these are achieved by a 3D restricted uniform scenario and design the array topology accordingly. This is because the 3D restricted uniform scenario requires more antenna array space, hence, analysis will cover the 3D Gaussian scenario too.

C. Design of Optimized Antenna Array Topologies

We further devise optimized antenna array topologies achieving maximum capacity and occupying minimum space for a given number of array elements and AOA distribution using the PSOvm algorithm. We focus on spherical arrays, as linear and circular topologies can be optimum too should we know the subtended SDoF and occupied space, see Figs. 4, 5. We consider a 10×10 MIMO system, i.e., having equal to $X = 10$ elements at both the transmitter and receiver sides. The array space limits for all propagation scenarios are seen in Table III. We let the PSO particles search on the space boundaries of spherical arrays and running the PSOvm algorithm we find the element positions for spherical array topologies in each propagation scenario. As an example, in Fig. 7, we

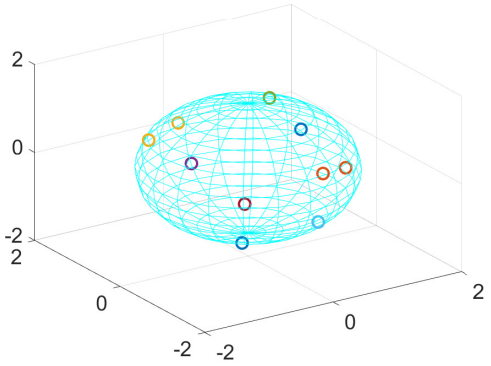

Fig. 7. Optimized spherical array topology in the 3D Gaussian (variance) scenario.

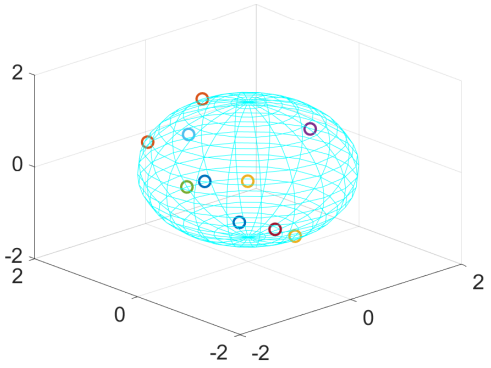

Fig. 8. Optimized arbitrarily-shaped array topology in the 3D Gaussian (variance) scenario.

demonstrate such optimum topology for the 3D Gaussian (variance) scenario. The achieved maximum capacities in each propagation scenario are listed in Table IV. We observe that the achieved capacities of all spherical array topologies are almost equal to the theoretical maximum one. Similar observations are reported in Table IV when applying the optimization algorithm to linear and circular array topologies. Using the array density metric as the number or array elements per unit area, i.e., $D_A = N_A/S$ [16], with $N_A = 10$ elements and S the occupied area, we obtain $D_A = 0.37$ elements/λ^2, $D_A = 0.20$ elements/λ^2 for the spherical (Fig. 7) and circular (see Table III) arrays, respectively. Thus, in the 3D Gaussian (variance) scenario, the spherical array of Fig. 7 is more space efficient than the circular one by 85%, i.e., it has 85% more elements in the same area.

In an attempt to further minimize the occupied space of antenna arrays, we release the limitation of letting the particles to search on the boundaries only. We run the algorithm by arbitrarily positioning the array elements. Thus, we let the particles search inside the spherical space considering the same limits as in previous spherical topologies (see Table III). In all propagation scenarios, most array elements tend to stay on the boundary of the spherical topology and such antenna arrays approach the maximum theoretical capacity (see Table IV). This seems a natural selection in order the array elements to occupy positions in space achieving such inter-element distancing that minimizes the spatial correlation between them and eventually maximizes the ergodic MIMO channel capacity.

It thus validates that the space constraint determined by our SDoF formulation is the minimum occupied space. In other words, the particles of the algorithm can be directly set to search on the array boundary instead of searching inside the whole space. As an example, we demonstrate the optimum topology in Fig. 8 for the 3D Gaussian (variance) scenario. In both Figs. 7, 8, the optimum array topologies are non-uniform as a result of directional 3D AOA distributions.

VII. Conclusion

We generalized the SDoF formulations for linear, circular, and spherical arrays in all classes of propagation scenarios, namely, isotropic, directional, and omnidirectional, by using the differential entropy of 3D AOA distributions. Such SDoF formulations can be used to either determine the maximum number of array elements for a given spatial constraint (as in [15]), or limit the array space to allocate a certain amount of elements ensuring optimum ergodic MIMO channel capacity performance. An advanced PSOvm algorithm was employed to maximize capacity incorporating novel closed-form SCFs. Such SCFs rely on a generic system model applicable to any antenna array topology including arbitrarily-shaped topologies. The proposed SDoF informed the design of optimized antenna array topologies achieving maximum capacity while occupying minimum space. The presented SDoF formulations can be readily extended to any AOA distribution, including distributions for more complex multi-clustered propagation. Extension to wireless environments incorporating diffuse (rich) scattering and specular components would require a different mathematical treatise as the AOA distribution would comprise of a mixture of continuous and discrete functions. The presented sequential approach, i.e., closed-form SCF derivation, SDoF formulation, and ergodic MIMO channel capacity maximization, can constitute a roadmap for future antenna array designs towards implementing 6G wireless systems with volumetric spectral efficiency [7] and adopting 3D antenna arrays in 3GPP standardization efforts [8]. It can further inspire information theorists attempting to associate their work with wireless propagation [5].

Appendix A
Proof of (13)

Substituting (5) into (12), using (6) and (7), letting $\tilde{\phi} = \phi - \alpha_{m,n}$, the SCF of (12) can be written after some algebraic manipulations as

$$R_s(m,n) = \frac{1}{4\Delta\phi\cos\theta_0\sin\Delta\theta}\times \int_{\theta_0-\Delta\theta}^{\theta_0+\Delta\theta} \exp\left\{j\frac{2\pi}{\lambda}r_{m,n}\sin(\theta)\sin(\beta_{m,n})\right\}\cos(\theta)d\theta\times \int_{\phi_0-\Delta\phi-\alpha_{m,n}}^{\phi_0+\Delta\phi-\alpha_{m,n}} \exp\left\{j\frac{2\pi}{\lambda}r_{m,n}\cos(\theta)\cos(\beta_{m,n})\cos(\tilde{\phi})\right\}d\tilde{\phi}. \tag{45}$$

Following the Jacobi-Anger expansion rule [43], we have

$$e^{jz\cos(X)} = J_0(z) + 2\sum_{g=1}^{\infty} j^g J_g(z)\cos(gX). \tag{46}$$

Using (46) for the second integration of (45), we have after some manipulations

$$\begin{aligned}\int_{\phi_0-\Delta\phi-\alpha_{m,n}}^{\phi_0+\Delta\phi-\alpha_{m,n}} &\exp\left\{j2\pi r_{m,n}\cos(\theta)\cos(\beta_{m,n})\cos(\tilde{\phi})/\lambda\right\}d\tilde{\phi}\\ &= 2\Delta\phi J_0(j2\pi r_{m,n}\cos(\theta)\cos(\beta_{m,n})/\lambda)\\ &\quad + 4\Delta\phi\sum_{g=1}^{\infty}\{j^g J_g\left(j2\pi r_{m,n}\cos(\theta)\cos(\beta_{m,n})/\lambda\right)\\ &\quad\times\cos\left(g(\phi_0-\alpha_{m,n})\right)\mathrm{sinc}(g\Delta\phi)\}\end{aligned} \tag{47}$$

in which $\mathrm{sinc}(g\Delta\phi) = \sin(g\Delta\phi)/(g\Delta\phi)$. Substituting (47) into (45) yields

$$\begin{aligned}R_s(m,n) &= \frac{1}{2\cos\theta_0\sin\Delta\theta}\\ &\times\int_{\theta_0-\Delta\theta}^{\theta_0+\Delta\theta}\exp\{j2\pi r_{m,n}\sin(\theta)\sin(\beta_{m,n})/\lambda\}\cos(\theta)\\ &\times J_0\left(j2\pi r_{m,n}\cos(\theta)\cos(\beta_{m,n})/\lambda\right)d\theta\\ &+2\sum_{g=1}^{\infty}\int_{\theta_0-\Delta\theta}^{\theta_0+\Delta\theta}\exp\{j2\pi r_{m,n}\sin(\theta)\sin(\beta_{m,n})/\lambda\}\cos(\theta)\\ &\times J_g\left(j2\pi r_{m,n}\cos(\theta)\cos(\beta_{m,n})/\lambda\right)\\ &\quad\times j^g\cos\left(g(\phi_0-\alpha_{m,n})\right)\mathrm{sinc}(g\Delta\phi)d\theta.\end{aligned} \tag{48}$$

The trapezoidal rule [10] provides

$$\int_a^b f(Z)dZ \approx \frac{b-a}{Q}\times [0.5f(Z_0)+f(Z_1)+...+f(Z_{Q-1})+0.5f(Z_Q)] \tag{49}$$

where Z_Q denotes the Q-th partition of the integration interval in Trapezoidal rule. In (48), we let

$$\begin{aligned}f_0(\Theta) &= \exp\left[j2\pi r_{m,n}\sin(\beta_{m,n})\sin(\Theta)/\lambda\right]\cos(\Theta)\\ &\quad\times J_0\left(2\pi r_{m,n}\cos(\beta_{m,n})\cos(\Theta)/\lambda\right)\end{aligned} \tag{50}$$

$$\begin{aligned}f_g(\Theta) &= \exp\left[j2\pi r_{m,n}\sin(\beta_{m,n})\sin(\Theta)/\lambda\right]\cos(\Theta)\\ &\quad\times J_g\left(2\pi r_{m,n}\cos(\beta_{m,n})\cos(\Theta)/\lambda\right)\end{aligned} \tag{51}$$

where $J_0(.)$ and $J_g(.)$, $g = 1, 2, ..., G$, are the zero-order and the g-order Bessel functions of the first kind, respectively. Substituting (49), (50) and (51) into (48), we obtain (13).

Appendix B
Proof of (17)

Let $A = A_1 \times A_2$. Substituting (5) into (12) and using (6), (8), after some manipulations, the SCF of (12) can be expressed as

$$\begin{aligned}R_s(m,n) &= \frac{A}{2\pi\sigma_\theta\sigma_\phi}\\ &\times\int_\theta\int_\phi\exp\left[-\left(\frac{\theta-\theta_0}{\sqrt{2}\sigma_\theta}\right)^2\right]\exp\left[-\left(\frac{\phi-\phi_0}{\sqrt{2}\sigma_\phi}\right)^2\right]\\ &\quad\times\exp\{j2\pi r_{m,n}\cos(\theta)\cos(\beta_{m,n})\cos(\alpha_{m,n}-\phi)/\lambda\}\\ &\quad\times\exp\{j2\pi r_{m,n}\sin(\theta)\sin(\beta_{m,n})/\lambda\}\cos(\theta)d\phi d\theta\end{aligned} \tag{52}$$

where $\theta\in[-\pi/2,\pi/2]$, $\phi\in[-\pi/2+\phi_0,\pi/2+\phi_0]$. Letting $x_q = (\theta-\theta_0)/(\sqrt{2}\sigma_\theta)$, $x_p = (\phi-\phi_0)/(\sqrt{2}\sigma_\phi)$, we have

$\theta = \sqrt{2}\sigma_\theta x_q + \theta_0$, $\phi = \sqrt{2}\sigma_\phi x_p + \phi_0$, and after some manipulations, the SCF in (52) can be approximated as [14], [49]

$$\begin{aligned} R_s(m,n) \approx & \frac{A}{\pi} \times \\ & \int_{x_q} e^{-x_q^2} \exp\left\{ j2\pi r_{m,n} \sin(\sqrt{2}\sigma_\theta x_q + \theta_0) \sin(\beta_{m,n})/\lambda \right\} \times \\ & \cos(\sqrt{2}\sigma_\theta x_q + \theta_0) \int_{x_p} e^{-x_p^2} \exp\left\{ j2\pi r_{m,n} \cos(\sqrt{2}\sigma_\theta x_q + \theta_0) \right. \\ & \left. \times \cos(\beta_{m,n}) \cos(\alpha_{m,n} - \sqrt{2}\sigma_\phi x_p - \phi_0)/\lambda \right\} dx_p dx_q. \end{aligned} \tag{53}$$

Using (15) in (53) yields (17).

APPENDIX C
PROOF OF (18)

Substituting (5) into (12), and using (6), (11), (47) with $\phi_0 = 0$, $\Delta\phi = \pi$, the SCF of (12) can be expressed after some manipulations as

$$\begin{aligned} R_s(m,n) = & \frac{A_1}{2\pi\sqrt{2\pi}\sigma_\theta} \int_\theta \exp\left\{ j\frac{2\pi}{\lambda} r_{m,n} \sin(\theta) \sin(\beta_{m.n}) \right\} \\ & \times \exp\left[-\left(\frac{\theta - \theta_0}{2\sigma_\theta^2} \right)^2 \right] \cos(\theta) \\ & \times 2\pi J_0\left(j\frac{2\pi}{\lambda} r_{m,n} \cos(\theta) \cos(\beta_{m,n}) \right) d\theta. \end{aligned} \tag{54}$$

By letting $\theta = \sqrt{2}\sigma_\theta x_q + \theta_0$, (54) can be approximated as [14], [49]

$$\begin{aligned} R_s(m,n) \approx & \frac{A_1}{\sqrt{\pi}} \times \\ & \int_{x_q} e^{-x_q^2} \exp\left\{ j\frac{2\pi}{\lambda} r_{m,n} \sin(\sqrt{2}\sigma_\theta x_q + \theta_0) \sin(\beta_{m,n}) \right\} \\ & \times \cos(\sqrt{2}\sigma_\theta x_q + \theta_0) \\ & \times J_0\left(j2\pi r_{m,n} \cos(\sqrt{2}\sigma_\theta x_q + \theta_0) \cos(\beta_{m,n})/\lambda \right) dx_q. \end{aligned} \tag{55}$$

Using (15) in (55) yields (18).

APPENDIX D
PROOF OF (27), (28), (29) AND (30), (33), (34)

A. SDoF for 3D Restricted Uniform Scenarios

Substituting (7) into (26), we obtain after some manipulations

$$H_u(\theta, \phi) = \log_2(4\Delta\phi \cos\theta_0 \sin\Delta\theta). \tag{56}$$

Substituting (56) into $2^{H_u(\theta,\phi)}$ results in (27).

After some manipulations, (27) can be written as follows

$$H_u(\theta, \phi) = H_u(\theta) + H_u(\phi) \tag{57}$$

where $H_u(\theta)$ and $H_u(\phi)$ are defined as

$$H_u(\theta) = -\int_\theta \cos\theta P_u(\theta) \log_2 P_u(\theta) d\theta, \tag{58}$$

$$H_u(\phi) = -\int_\phi P_u(\phi) \log_2 P_u(\phi) d\phi. \tag{59}$$

Using $P_u(\theta)$ and $P_u(\phi)$ (see below (7)) in (58) and (59), respectively, we have

$$H_u(\theta) = \log_2(2\cos\theta_0 \sin\Delta\theta), \tag{60}$$

$$H_u(\phi) = \log_2(2\Delta\phi). \tag{61}$$

Substituting (60), (61) into $2^{H_u(\theta)}$, $2^{H_u(\phi)}$, respectively, we obtain (28), (29).

B. SDoF for 3D Gaussian Scenarios

Substituting (8) into (26), we obtain after some manipulations

$$\begin{aligned} & H_{Gau}(\theta, \phi) = \\ & \log_2\left(\frac{\sqrt{2\pi}\sigma_\theta}{A_1} \right) \int_\theta \cos\theta P_{Gau}(\theta) d\theta \int_\phi P_{Gau}(\phi) d\phi \\ & + \frac{log_2 e}{2\sigma_\theta^2} \int_\theta \cos\theta P_{Gau}(\theta)(\theta - \theta_0)^2 d\theta \int_\phi P_{Gau}(\phi) d\phi \\ & + \log_2\left(\frac{\sqrt{2\pi}\sigma_\phi}{A_2} \right) \int_\theta \cos\theta P_{Gau}(\theta) d\theta \int_\phi P_{Gau}(\phi) d\phi \\ & + \frac{log_2 e}{2\sigma_\phi^2} \int_\theta \cos\theta P_{Gau}(\theta) d\theta \int_\phi P_{Gau}(\phi)(\phi - \phi_0)^2 d\phi. \end{aligned} \tag{62}$$

Using $\int_\phi P_{Gau}(\phi) d\phi = 1$, $\int_\theta \cos\theta P_{Gau}(\theta) d\theta = 1$ and substituting (31), (32) into (62), we obtain after some manipulations

$$\begin{aligned} & H_{Gau}(\theta, \phi) = \\ & \log_2 \frac{2\pi\sigma_\theta\sigma_\phi}{A_1 A_2} + \log_2 \exp\left[\frac{\sigma_\phi^2 V_{Gau}(\theta) + \sigma_\theta^2 V_{Gau}(\phi)}{2\sigma_\theta^2 \sigma_\phi^2} \right]. \end{aligned} \tag{63}$$

Substituting (63) into $2^{H_{Gau}(\theta,\phi)}$ results in (30).

After some manipulations, (26) can be written as follows

$$H_{Gau}(\theta, \phi) = H_{Gau}(\theta) + H_{Gau}(\phi) \tag{64}$$

where $H_{Gau}(\theta)$ and $H_{Gau}(\phi)$ can be defined as

$$H_{Gau}(\theta) = -\int_\theta \cos\theta P_{Gau}(\theta) \log_2 P_{Gau}(\theta) d\theta, \tag{65}$$

$$H_{Gau}(\phi) = -\int_\phi P_{Gau}(\phi) \log_2 P_{Gau}(\phi) d\phi. \tag{66}$$

After some manipulations, (65) and (66) can be written as follows

$$H_{Gau}(\theta) = \log_2\left\{ \frac{\sqrt{2\pi}\sigma_\theta}{A_1} \exp\left[\frac{V_{Gau}(\theta)}{2\sigma_\theta^2} \right] \right\}, \tag{67}$$

$$H_{Gau}(\phi) = \log_2\left\{ \frac{\sqrt{2\pi}\sigma_\phi}{A_2} \exp\left[\frac{V_{Gau}(\phi)}{2\sigma_\phi^2} \right] \right\}. \tag{68}$$

Substituting (67), (68) into $2^{H_{Gau}(\theta)}$, $2^{H_{Gau}(\phi)}$, respectively, we obtain (33), (34).

REFERENCES

[1] M. Shafi, A. F. Molisch, P. J. Smith, T. Haustein, P. Zhu, P. De Silva, F. Tufvesson, A. Benjebbour, and G. Wunder, "5G: A Tutorial Overview of Standards, Trials, Challenges, Deployment, and Practice," *IEEE Journal on Selected Areas in Communications*, vol. 35, no. 6, pp. 1201–1221, 2017.

[2] A. Paulraj, R. Nabar, and D. Gore, *Introduction to Space-Time Wireless Communications*. Cambridge University Press, 2008.

[3] C. T. Neil, A. Garcia-Rodriguez, P. J. Smith, P. A. Dmochowski, C. Masouros, and M. Shafi, "On the Performance of Spatially Correlated Large Antenna Arrays for Millimeter-Wave Frequencies," *IEEE Transactions on Antennas and Propagation*, vol. 66, no. 1, pp. 132–148, 2018.

[4] D.-S. Shiu, G. Foschini, M. Gans, and J. Kahn, "Fading Correlation and Its Effect on the Capacity of Multielement Antenna Systems," *IEEE Transactions on Communications*, vol. 48, no. 3, pp. 502–513, 2000.

[5] M. Franceschetti, *Wave Theory of Information*. Cambridge University Press, 2017.

[6] L. Zheng and D. Tse, "Diversity and Multiplexing: A Fundamental Tradeoff in Multiple-Antenna Channels," *IEEE Transactions on Information Theory*, vol. 49, no. 5, pp. 1073–1096, 2003.

[7] W. Saad, M. Bennis, and M. Chen, "A Vision of 6G Wireless Systems: Applications, Trends, Technologies, and Open Research Problems," *IEEE Network*, vol. 34, no. 3, pp. 134–142, 2020.

[8] 3GPP TR 38.901, "Study on Channel Model for Frequencies From 0.5 to 100 GHz (Release 16)," 3GPP, Tech. Rep., Nov 2020.

[9] S. K. Yong and J. Thompson, "Three-Dimensional Spatial Fading Correlation Models for Compact MIMO Receivers," *IEEE Transactions on Wireless Communications*, vol. 4, no. 6, pp. 2856–2869, 2005.

[10] J.-H. Lee and C.-C. Cheng, "Spatial Correlation of Multiple Antenna Arrays in Wireless Communication Systems," *Progress In Electromagnetics Research*, vol. 132, pp. 347–368, 2012.

[11] Y. F. Alem, Z. Khalid, and R. A. Kennedy, "3D Spatial Fading Correlation for Uniform Angle of Arrival Distribution," *IEEE Communications Letters*, vol. 19, no. 6, pp. 1073–1076, 2015.

[12] P. Teal, T. Abhayapala, and R. Kennedy, "Spatial Correlation for General Distributions of Scatterers," *IEEE Signal Processing Letters*, vol. 9, no. 10, pp. 305–308, 2002.

[13] H. Jiang, D. Tang, J. Zhou, X. Xi, J. Feng, J. Dang, and L. Wu, "Approximation Algorithm Based Channel Estimation for Massive MIMO Antenna Array Systems," *IEEE Access*, vol. 7, pp. 149 364–149 372, 2019.

[14] L. Zhang, Z. Luo, and S.-H. Leung, "An Efficient Approximation of Spatial Correlation Based on Gauss–Hermite Quadrature," *IEEE Transactions on Signal Processing*, vol. 66, no. 3, pp. 617–626, 2018.

[15] A. Poon, R. Brodersen, and D. Tse, "Degrees of Freedom in Multiple-Antenna Channels: a Signal Space Approach," *IEEE Transactions on Information Theory*, vol. 51, no. 2, pp. 523–536, 2005.

[16] S. M. Mikki, S. Clauzier, and Y. M. M. Antar, "Empirical Geometrical Bounds on MIMO Antenna Arrays for Optimum Diversity Gain Performance: An Electromagnetic Design Approach," *IEEE Access*, vol. 6, pp. 39 876–39 894, 2018.

[17] H. Do, N. Lee, and A. Lozano, "Reconfigurable ULAs for Line-of-Sight MIMO Transmission," *IEEE Transactions on Wireless Communications*, vol. 20, no. 5, pp. 2933–2947, 2021.

[18] W. Liu and Z. Wang, "Non-Uniform Full-Dimension MIMO: New Topologies and Opportunities," *IEEE Wireless Communications*, vol. 26, no. 2, pp. 124–132, 2019.

[19] P. Karadimas and J. Zhang, "A Generalized Analysis of Three-Dimensional Anisotropic Scattering in Mobile Wireless Channels-Part I: Theory," in *2011 IEEE 73rd Vehicular Technology Conference (VTC Spring)*, 2011, pp. 1–5.

[20] T. Taga, "Analysis for Mean Effective Gain of Mobile Antennas in Land Mobile Radio Environments," *IEEE Transactions on Vehicular Technology*, vol. 39, no. 2, pp. 117–131, 1990.

[21] A. Ando, T. Taga, A. Kondo, K. Kagoshima, and S. Kubota, "Mean Effective Gain of Mobile Antennas in Line-of-Sight Street Microcells With Low Base Station Antennas," *IEEE Transactions on Antennas and Propagation*, vol. 56, no. 11, pp. 3552–3565, 2008.

[22] K. Kalliola, K. Sulonen, H. Laitinen, O. Kivekas, J. Krogerus, and P. Vainikainen, "Angular Power Distribution and Mean Effective Gain of Mobile Antenna in Different Propagation Environments," *IEEE Transactions on Vehicular Technology*, vol. 51, no. 5, pp. 823–838, 2002.

[23] U. Olgun, C. A. Tunc, D. Aktas, V. B. Erturk, and A. Altintas, "Optimization of Linear Wire Antenna Arrays to Increase MIMO Capacity Using Swarm Intelligence," in *The Second European Conference on Antennas and Propagation, EuCAP 2007*, 2007, pp. 1–6.

[24] M. O. Binelo, A. L. F. de Almeida, and F. R. P. Cavalcanti, "MIMO Array Capacity Optimization Using a Genetic Algorithm," *IEEE Transactions on Vehicular Technology*, vol. 60, no. 6, pp. 2471–2481, 2011.

[25] W. Chien, C.-C. Chiu, Y.-T. Cheng, S.-H. Liao, and H.-S. Yen, "Multi-Objective Optimization for UWB Antenna Array by APSO Algorithm," *Telecommunication Systems*, vol. 64, no. 4, pp. 649–660, 2017.

[26] A. Reyna, J. C. Garza, O. Elizarraras, M. Panduro, L. I. Balderas, and M. d. l. L. Prado, "3D Random Virtual Antenna Arrays for FANETs Wireless Links," *Telecommunication Systems*, vol. 77, no. 3, pp. 469–477, 2021.

[27] X. Zhang and X. Zhang, "Thinning of Antenna Array via Adaptive Memetic Particle Swarm Optimization," *EURASIP Journal on Wireless Communications and Networking*, vol. 2017, no. 1, pp. 1–7, 2017.

[28] H. Yongqiang, L. Wentao, and L. Xiaohui, "Particle Swarm Optimization for Antenna Selection in MIMO System," *Wireless Personal Communications*, vol. 68, no. 3, pp. 1013–1029, 2013.

[29] Y. Rahmat-Samii, "Modern Antenna Designs using Nature Inspired Optimization Techniques: Let Darwin and the bees help designing your multi band MIMO antennas," in *2007 IEEE Radio and Wireless Symposium*, 2007, pp. 463–466.

[30] Z. D. Zaharis, I. P. Gravas, P. I. Lazaridis, I. A. Glover, C. S. Antonopoulos, and T. D. Xenos, "Optimal LTE-Protected LPDA Design for DVB-T Reception Using Particle Swarm Optimization With Velocity Mutation," *IEEE Transactions on Antennas and Propagation*, vol. 66, no. 8, pp. 3926–3935, 2018.

[31] M. D. Migliore, "On Electromagnetics and Information Theory," *IEEE Transactions on Antennas and Propagation*, vol. 56, no. 10, pp. 3188–3200, 2008.

[32] K. Haneda, A. Khatun, M. Dashti, T. A. Laitinen, V.-M. Kolmonen, J.-I. Takada, and P. Vainikainen, "Measurement-Based Analysis of Spatial Degrees of Freedom in Multipath Propagation Channels," *IEEE Transactions on Antennas and Propagation*, vol. 61, no. 2, pp. 890–900, 2013.

[33] H. Zhang, R. He, B. Ai, S. Cui, and H. Zhang, "Measuring Sparsity of Wireless Channels," *IEEE Transactions on Cognitive Communications and Networking*, vol. 7, no. 1, pp. 133–144, 2021.

[34] S. Sun and H. Yan, "Small-Scale Spatial-Temporal Correlation and Degrees of Freedom for Reconfigurable Intelligent Surfaces," *IEEE Wireless Communications Letters*, vol. 10, no. 12, pp. 2698–2702, 2021.

[35] A. Pizzo, A. d. J. Torres, L. Sanguinetti, and T. L. Marzetta, "Nyquist Sampling and Degrees of Freedom of Electromagnetic Fields," *IEEE Transactions on Signal Processing*, vol. 70, pp. 3935–3947, 2022.

[36] T. M. Cover and J. A. Thomas, *Elements of Information Theory, 2nd Edition*. Wiley-Interscience, 2006.

[37] Y. K. Huang, P. Karadimas, and A. P. Sohrab, "Multi-Antenna Array Topologies Optimization for Future Wireless Networks by Employing Particle Swarm Optimization," in *2019 PhotonIcs & Electromagnetics Research Symposium - Spring (PIERS-Spring)*, 2019, pp. 4138–4143.

[38] A. Grant, "Rayleigh Fading Multi-Antenna Channels," *EURASIP Journal on Advances in Signal Processing*, vol. 2002, no. 3, pp. 1–14, 2002.

[39] B. Han and Y. R. Zheng, "Higher Rank Principal Kronecker Model for Triply Selective Fading Channels With Experimental Validation," *IEEE Transactions on Vehicular Technology*, vol. 64, no. 5, pp. 1654–1663, 2015.

[40] E. Telatar, "Capacity of Multi-Antenna Gaussian Channels," *European Transactions on Telecommunications*, vol. 10, no. 6, pp. 585–595, 1999.

[41] W. Weichselberger, M. Herdin, H. Ozcelik, and E. Bonek, "A Stochastic MIMO Channel Model with Joint Correlation of Both Link Ends," *IEEE Transactions on Wireless Communications*, vol. 5, no. 1, pp. 90–100, 2006.

[42] H. L. Van Trees, *Optimum Array Processing: Part IV of Detection, Estimation, and Modulation Theory*. John Wiley & Sons, 2004.

[43] M. Abramowitz and I. A. Stegun, *Handbook of Mathematical Functions with Formulas, Graphs, and Mathematical Tables*. Dover Publications, Inc., New York, 1972.

[44] B. Fleury, "First- and Second-Order Characterization of Direction Dispersion and Space Selectivity in the Radio Channel," *IEEE Transactions on Information Theory*, vol. 46, no. 6, pp. 2027–2044, 2000.

[45] J. Robinson and Y. Rahmat-Samii, "Particle Swarm Optimization in Electromagnetics," *IEEE Transactions on Antennas and Propagation*, vol. 52, no. 2, pp. 397–407, 2004.

[46] A. Carlisle and G. Dozier, "An Off-the-Shelf PSO. Proceedings of the Workshop on Particle Swarm Optimization," *Purdue School of Engineering and Technology, Indianapolis, IN*, 2001.

[47] Eberhart and Y. Shi, "Particle Swarm Optimization: Developments, Applications and Resources," in *Proceedings of the 2001 Congress on*

Evolutionary Computation (IEEE Cat. No.01TH8546), vol. 1, 2001, pp. 81–86 vol. 1.

[48] D. Zwillinger and A. Jeffrey, *Table of Integrals, Series, and Products*. Elsevier, 2014.

[49] C. Walck, *Hand-Book on Statistical Distributions for Experimentalists*. University of Stockholm, 2007.